Pergamon

Int. J. Heat Mass Transfer. Vol. 39, No. 13, pp. 2699–2710, 1996

0017-9310/96 $15.00+0.00

0017-9310(95)00364-9

A bifurcation study of double diffusive flows in a laterally heated stably stratified liquid layer

H. A. DIJKSTRA and E. J. KRANENBORG

Institute for Marine and Atmospheric Research, Utrecht University, Utrecht, The Netherlands

(*Received* 5 *January* 1995 *and in final form* 26 *September* 1995)

Abstract—The double diffusive layer formation process in a laterally heated liquid layer which is stably stratified through a constant vertical salinity gradient is considered. The salt field is fixed at the horizontal boundaries to allow for steady solutions. The structure of stationary solutions and their linear stability is determined using continuation methods. Boundaries between different flow regimes, as observed experimentally, are to some extent identified as paths of particular bifurcation points. Using time integrations it is shown that unstable steady-states are physically relevant because the time at which the particular instability sets in may be very long. Copyright © 1996 Elsevier Science Ltd.

1. INTRODUCTION

When a lateral temperature gradient is applied to a motionless liquid layer which is stably stratified through a constant vertical salinity gradient ϕ_0, a buoyancy driven flow appears. This flow may become unstable when a critical value of the lateral temperature gradient is exceeded. The instabilities are shear driven for small ϕ_0, but when ϕ_0 is large the flow becomes unstable to double diffusive instabilities. The latter are due to the different thermal and solutal diffusivities. When a parcel of liquid near the heated wall moves upward, it retains almost all of its salt due to its very small diffusivity, but loses its heat relatively fast. The parcel rises to a level where its density is equal to that of the surrounding liquid and because of continuity it is then forced to move laterally; a layered flow pattern results.

The vertical temperature and salinity structures associated with these layers show characteristic step-like structures. Such step structures in temperature and salinity have been found over large areas in the upper ocean. Since the presence of layers significantly influences the transport of heat and salt, double diffusive convection is a potentially important transport mechanism, e.g. for heat and salt in the ocean [1]. Apart from the oceanographic context, there are many technological motivations to study these type of flows, for example crystal growth and the heat storage in solar ponds.

Much information on the layer formation process was obtained from laboratory experiments. These were performed either in narrow slots or in wide tanks. They differ also in the way the heating is imposed at the lateral walls, for example very slowly [2] or through a particular time dependence [3–5]. In most of the experiments, three stages of flow development are observed. There is an initial stage characterized either by spontaneous cell formation along the heated wall or by flow developing from the horizontal boundaries. In the latter flows, the cells at the horizontal boundaries penetrate towards the center of the cavity during the second stage of evolution. In the first type of flows, layers merge during the second stage leading to an increase in the average thickness of the layers. Eventually, in both cases, a quasi-steady pattern forms with a layered structure over the whole container. Good sets of pictures showing these three stages can, for example, be found in ref. [4].

The experiments indicate that there is a boundary in parameter space separating these two qualitatively different regimes of flow. In ref. [3], a boundary in parameter space was proposed as the critical value of a Rayleigh number Ra_η based on the length scale

$$\eta = \frac{\alpha \Delta T}{\beta \phi_0}. \tag{1}$$

Here ΔT is the laterally imposed temperature difference and α, β the thermal and solutal expansion coefficients, respectively. The length scale η is directly related to the movement of a heated liquid parcel to its neutrally buoyant level. It was found [3] that when Ra_η exceeds a critical value given approximately by $Ra_{\eta,\mathrm{cr}} = 1.5 \times 10^4$, the layers formed simultaneously. In this case, a layered convection pattern with a vertical lengthscale η is developed [4, 6, 7]. Below the critical value the layers grow successively from the horizontal walls, and layers with a larger scale may develop.

Theoretical work has mainly focused on the initial stage of layer formation as an instability of a weak buoyancy driven background flow. In the ideal situation of a vertically unbounded layer this flow is parallel, with liquid rising near the hot wall and descending along the cold wall. The parallel flow can be calculated analytically [8] and at large salinity gradient ϕ_0, it can

NOMENCLATURE

A	aspect ratio equation (9)
g	gravitational acceleration [m s^{-2}]
H	height of the container [m]
J	Jacobian equation (6)
L	length of container [m]
L_1	limit point
Le	Lewis number equation (9)
P_1, P_2	bifurcation points
Pr	Prandtl number equation (9)
R_ρ	buoyancy ratio equation (9)
Ra_η	thermal Rayleigh number based on η
Ra_S	solutal Rayleigh number equation (10)
Ra_T	thermal Rayleigh number equation (9)
Ri	Richardson number
S	dimensionless salinity
S^*	salinity
T	dimensionless temperature
T^*	temperature [K]
u	dimensionless horizontal velocity
w	dimensionless vertical velocity.

Greek symbols

α	thermal expansion coefficient [K^{-1}]
β	solutal expansion coefficient
ΔT	lateral temperature difference [K]
ΔS	vertical salinity difference
η	internal vertical lengthscale [m]
ϕ_0	initial salinity gradient [m^{-1}]
κ_T	thermal diffusivity [m^2 s^{-1}]
κ_S	saline diffusivity [m^2 s^{-1}]
λ	exponential growth factor
μ	viscosity [kg m^{-1} s^{-1}]
ν	kinematic viscosity [m^2 s^{-1}]
ρ	density [kg m^{-3}]
τ_S	salt diffusion time scale [s]
ω	dimensionless vorticity
ψ	dimensionless streamfunction
ψ_0	streamfunction at a particular gridpoint.

Subscripts

cr	critical
0	reference value
m	maximum value.

be shown to be unstable to double diffusive instabilities for a sufficiently large lateral temperature gradient. A rigorous series of studies on the instability of the boundary layer due to a gradually heated wall has been performed by Kerr [9, 10]. He demonstrated that for this case, the instability is oscillatory and that finite amplitude flows exist below the instability boundary (although these were found to be unstable).

In this paper, we focus on the long time behavior of double diffusive layered flows in a narrow slot. The question we try to answer is whether the different flow regimes are related to a change in attractive regions in phase space of the governing system of equations. In that respect, the experimental results in Lee *et al.* [11] and numerical results in Lee and Hyun [12] are most relevant. In ref. [11], an experimental configuration was used for which the salt field at the horizontal walls was kept constant by using permeable membranes, maintaining a salinity difference ΔS between the walls. Here, real steady equilibria exist and can be calculated numerically in parameter space by solving for the steady equations directly. Apart from the above mentioned type of flows, which they called simultaneously formed layer flows (regime III) and successively formed layer flows (regime II), they also found two other regimes. At low buoyancy ratio $R_\rho = \beta\Delta S/\alpha\Delta T$, a unicellular flow pattern was found (regime IV) and at a very large buoyancy ratio, a very weak flow (or no flow at all) was found (regime I).

In addition to the aspect-ratio A of the liquid layer (ratio of length to depth), the Prandtl number and the Lewis number, two other parameters control the dynamics of the flow. These are the thermal Rayleigh number Ra_T based on the liquid height H (or Ra_η based on η) and the above mentioned buoyancy ratio R_ρ. The solutal Rayleigh number Ra_S is the product of Ra_T and R_ρ. The aspect-ratio, the Prandtl number and the Lewis number will be fixed throughout this study. The salt boundary conditions at the horizontal walls are chosen to allow for steady-states to exist (as in ref. [11]). We use techniques from numerical bifurcation theory to determine branches of steady solutions in the two-dimensional parameter space spanned by Ra_η and the buoyancy ratio R_ρ. In addition, some trajectories showing the evolution of the flow are computed by direct numerical simulation at particular locations in parameter space.

The main aim of this paper is to identify the boundaries between the different flow regimes as paths of particular bifurcation points in parameter space. The work leads to the stability boundary of the weak buoyancy driven nonparallel flow; this is a symmetry breaking bifurcation point. A lower bound for the successively layered flow regime is likely to be associated with a path of limit points on the asymmetric branch originating from this symmetry breaking bifurcation.

The boundary between the unicellular flow regime and that of the simultaneously formed layer regime is associated with the instability of the unicellular flow. Further identification could not be made due to an abundance of bifurcation points in several regions of parameter space.

2. FORMULATION AND NUMERICAL METHODS

A two-dimensional rectangular container (length L and height H) is filled with a Newtonian liquid with a constant thermal diffusivity κ_T and viscosity μ. A stable vertical salinity gradient is maintained within the liquid by imposing a constant salinity difference ΔS between the horizontal walls of the container; the vertical heat flux of these walls vanishes. A constant horizontal temperature difference ΔT is applied between the vertical walls, which are impervious to salt. The density ρ depends linearly on temperature and salinity and is given by $\rho = \rho_0(1-\alpha(T^*-T_0)+\beta(S^*-S_0))$, where the zero subscript refers to reference values. The governing equations are non-dimensionalized using scales H, H^2/κ_T and κ_T/H for length, time and velocity, respectively. A dimensionless temperature T and salinity S are defined by $T=(T^*-T_0)/\Delta T$ and $S=(S^*-S_0)/\Delta S$. In terms of the streamfunction ψ and vorticity ω, where

$$u=\frac{\partial\psi}{\partial z} \quad w=-\frac{\partial\psi}{\partial x} \quad \omega=-\nabla^2\psi \tag{2}$$

the full equations, with the usual Boussinesq approximation, are given by

$$Pr^{-1}\left(\frac{\partial\omega}{\partial t}+J(\omega,\psi)\right)=\nabla^2\omega+Ra_T\left(\frac{\partial T}{\partial x}-R_\rho\frac{\partial S}{\partial x}\right) \tag{3}$$

$$\frac{\partial T}{\partial t}+J(T,\psi)=\nabla^2 T \tag{4}$$

$$\frac{\partial S}{\partial t}+J(S,\psi)=Le^{-1}\nabla^2 S \tag{5}$$

where the Jacobian J is defined as

$$J(a,b)=\frac{\partial a}{\partial x}\frac{\partial b}{\partial z}-\frac{\partial a}{\partial z}\frac{\partial b}{\partial x}. \tag{6}$$

At all boundaries no-slip conditions for velocity are prescribed and for the temperature and salinity the following boundary conditions hold:

$$x=0: T=-\tfrac{1}{2} \quad \frac{\partial S}{\partial x}=0; \quad x=A: T=\tfrac{1}{2} \quad \frac{\partial S}{\partial x}=0 \tag{7}$$

$$z=0: S=1 \quad \frac{\partial T}{\partial z}=0; \quad z=1: S=0 \quad \frac{\partial T}{\partial z}=0. \tag{8}$$

The dimensionless parameters which appear in the equations above are defined as

$$Ra_T=\frac{g\alpha\Delta T H^3}{\nu\kappa_T} \quad R_\rho=\frac{\beta\Delta S}{\alpha\Delta T} \quad Pr=\frac{\mu}{\kappa_T\rho_0}$$

$$Le=\frac{\kappa_T}{\kappa_S} \quad A=\frac{L}{H} \tag{9}$$

and the solutal Rayleigh number is given by

$$Ra_S=Ra_T R_\rho=\frac{g\beta\Delta S H^3}{\nu\kappa_T}. \tag{10}$$

A relation between the Rayleigh numbers Ra_η, used in ref. [3], and Ra_T is $Ra_\eta=Ra_T/(R_\rho)^3$. Using $\partial S_0/\partial z=\Delta S/H$, a straightforward relation exists between the lengthscales H, η and the buoyancy ratio, i.e. $H/\eta=R_\rho$. In a liquid layer of height H, the solutions with characteristic length scale η therefore correspond to R_ρ cells.

The equations and boundary conditions were discretized using a finite volume finite difference method as in ref. [13]. We use three types of numerical codes to study the steady and transient solutions of the system of equations above. Steady-states and their linear stability are calculated as a function of the parameters using the continuation code presented in ref. [14]. A non-equidistant grid was used near the vertical boundaries in order to get an accurate representation of the boundary layers. No stretching was applied in z because in addition to the boundary layers at the horizontal walls, also large internal vertical gradients, in particular in salinity, may occur.

Two time-dependent numerical solvers, an explicit code using a fast Poisson solver and a fully implicit solver, were used. The first code has the advantage that it can be run at high resolution. However, its disadvantage is the restriction of the time step because of numerical instability. With the second code, larger time steps can be taken, but at lower resolution. Hence, the explicit code was used in the initial stage of the development of the flow and the implicit code in the approach to steady-state. The codes were verified using standard problems and the choice of resolution and time step was based on extensive testing of the accuracy of the solutions.

3. RESULTS FOR THE UNICELLULAR FLOW REGIME: $R_\rho = 3$

The Prandtl and Lewis numbers are fixed at values corresponding to the heat/salt system: $Pr = 6.7$, $Le = 101$ and the aspect-ratio A is fixed at $A = 1/2$. In a typical experiment in the unicellular flow regime, regime IV in ref. [11], first a four-cell pattern is observed, thereafter the cells merge until a two-cell state is reached and finally a one-cell solution is obtained, which appears to be a steady-state of the system. In this section, we first determine the steady-states of the system and subsequently study the time evolution towards the stable steady-states.

3.1. *Branches of steady solutions*

In these computations, we choose Ra_η as the bifurcation parameter; when this parameter is varied, both Ra_T and Ra_S vary. In Fig. 1 the bifurcation diagram for $Ra_\rho = 3$ is shown for relatively small Ra_η; this figure was computed using a $25 * 41$ grid. On the vertical axis, a value of the streamfunction at a particular gridpoint (ψ_0) is plotted, chosen to clearly distinguish

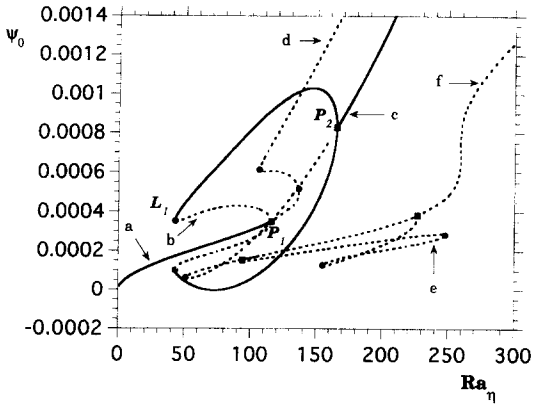

Fig. 1. Bifurcation diagram for $R_\rho = 3$ at small Ra_η. Note that the unstable branch starting at P_2 is not connected to P_1; the crossing is a visual effect caused by the particular choice of the monitor function ψ_0.

the different solution branches. Drawn (dotted) lines indicate stable (unstable) branches, and the bifurcation points are indicated by markers. A square is a pitchfork bifurcation and a dot indicates a limit point. Plots of the streamfunction and density are shown in Fig. 2, where the dimensionless density ρ is computed as $\rho = Ra_T(R\rho S - T)$.

When Ra_η is smaller than the value at L_1 in Fig. 1, there is a unique stable steady-state consisting of two cells [Fig. 2(a)], which rotate in the same direction (counterclockwise). With increasing Ra_η, this two-cell pattern becomes unstable through a subcritical pitchfork bifurcation at the point labeled P_1. This bifurcation is symmetry breaking and two branches of asymmetric solutions—but related through point-symmetry about the center of the cavity—appear. One of these solutions, a mixed one-cell/two-cell pattern, is shown in Fig. 2(b). Both asymmetric patterns remain unstable up to the limit point L_1, but stabilize with increasing Ra_η and remain stable up to the bifurcation point P_2. Along the branch $L_1 - P_2$, the flow pattern changes from a two-cell to a one-cell solution. For values of Ra_η larger than at P_2, the one-cell pattern is the only stable pattern [Fig. 2(c)]. The density is nearly homogeneous in the center of the container and there is a region of weakly (statically) unstable stratification. Along the symmetric branch which continues from P_1, the two-cell pattern is unstable. At larger Ra_η, both cells become separated by a relatively sharp interface, most clearly seen in the density distribution [Fig. 2(d)]. Within each cell, the density is nearly constant in the central region, while large gradients appear near the top and bottom. In regions of upward flow, advective salt transport increases the density upwards, causing smaller gradients downstream, but large ones upstream. In regions of downward flow, just the opposite occurs.

The branch coming down from P_2 also remains unstable. Along this branch, there are two other symmetry breaking bifurcation points. Here a curve of asymmetric solutions appears [an example is shown in Fig. 2(e)]; only one of these symmetry related branches is shown in Fig. 1. Along the symmetric branch, patterns appear with a slightly larger tilt and more cells at larger Ra_η. An example of a three-cell pattern, sandwiching two small cells, is shown in Fig. 2(f). The corresponding density plot shows that the regions of large gradients have disappeared, indicating that the temperature determines the spatial pattern of the density and that the salt is well mixed (except at the top and bottom). The tilt in the cells is caused by double diffusion; when the liquid moves away from the right (hot) wall, it looses its heat faster than its salt and therefore becomes heavier as the left wall is approached. The patterns along this part of the symmetric branch are all unstable.

In the small Ra_η regime, there are multiple stable steady-states over an interval $L_1 - P_2$ and unique stable steady-rates exist outside this interval (Fig. 1). Three branches extend into the region of larger Ra_η without any change in stability [Fig. 3(a)]. The gradients in both velocity [Fig. 3(b–d)] and density become stronger and more concentrated near the boundaries of a cell, including the interfaces between the cells. The salt is well mixed within each cell and very sharp salt gradients appear at the interfaces, giving a characteristic step structure in the vertical.

The increase in heat and salt transport due to convection was monitored by calculating the Nusselt number based on the heat flux through the vertical walls, and Sherwood number based on the salt flux through the horizontal walls. It appeared that both quantities are constant over the layer and are within 1%, as they should be for steady flow. Generally, transport increases [Fig. 4(a, b)] with Ra_η because, at constant R_ρ, Ra_η controls the total buoyant forcing. The numbers along the branches in Fig. 4 refer to the number of cells in the solution. As the number of cells increases they become smaller, allowing less vertical salt transfer because convection occurs on a smaller scale; this results in lower Sherwood numbers [Fig. 4(b)]. With an increasing number of cells the heat gain at the hot wall also decreases, which leads to a smaller horizontal heat transport resulting in a smaller Nusselt number [Fig. 4(a)].

Although there may be more branches of steady-states which do not connect to ones in the small forcing regime, a relatively simple bifurcation structure is found over a whole range of Ra_η. There is only one stable pattern, the one-cell solution, and one would expect long-term time-dependent calculations to approach this solution. This is in agreement with the numerical results in ref. [12], where a one-cell pattern was found for $R_\rho = 3$ and $Ra_T = 8.0 \times 10^7$ (corresponding to $Ra_\eta = 2.96 \times 10^6$). It is also in agreement with the experimental results in ref. [11] since the parameters here belong to those characterizing regime IV.

3.2. *Evolution towards steady-state*

The evolution of the flow in the cavity is studied from an initially motionless isothermal liquid which

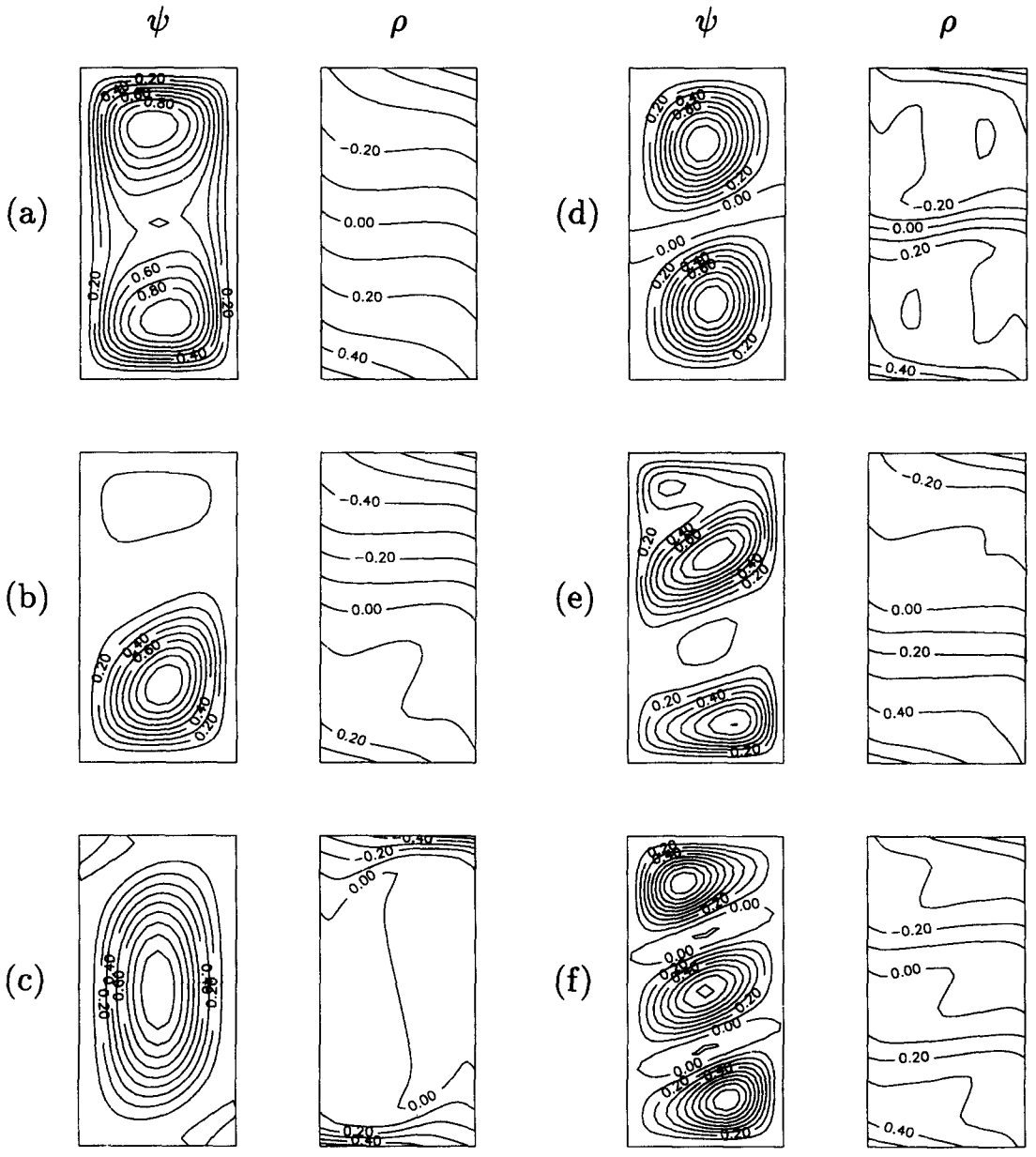

Fig. 2. Contour plots of the streamfunction and density at selected points in Fig. 1. For the density the value at the center is subtracted first. All contour levels are with respect to the maximum field.

is stably (salt) stratified. At $t = 0$ a constant horizontal temperature difference is imposed.

The initial conditions are

$$t \leqslant 0 : \psi = \omega = 0 ; S = 1 - z \tag{11}$$

$$t < 0 : T = 0 \tag{12}$$

$$t = 0 : T(x = 0) = -\tfrac{1}{2} ; T(x = A) = \tfrac{1}{2} \tag{13}$$

and are compatible with all boundary conditions. The $25 * 41$ grid used to determine the steady-states in Fig. 3 proved to be too coarse, because during the initial evolution smaller scale patterns appeared. It turned out that a $49 * 81$ grid gave sufficiently accurate results, in that doubling the spatial resolution and halving the time step did not show much difference over a chosen time interval. This grid size is comparable to that used in ref. [12].

For $Ra_\eta = 2.37 \times 10^4$ the evolution monitored by the maximum of the streamfunction ψ_m shows three different stages (Fig. 5). In the first stage, a four cell solution [Fig. 6(a)] is reached in a relatively short time. The vertical length scale of the convection cells is slightly smaller than η. Consistent with Fig. 3(a), where no four-cell stable steady solution was found, two pairs of cells merge as time progresses and a two-cell pattern forms [Fig. 6(b)]. Both the flow pattern and the corresponding density field hardly change over a long time interval (Fig. 5). However, the inte-

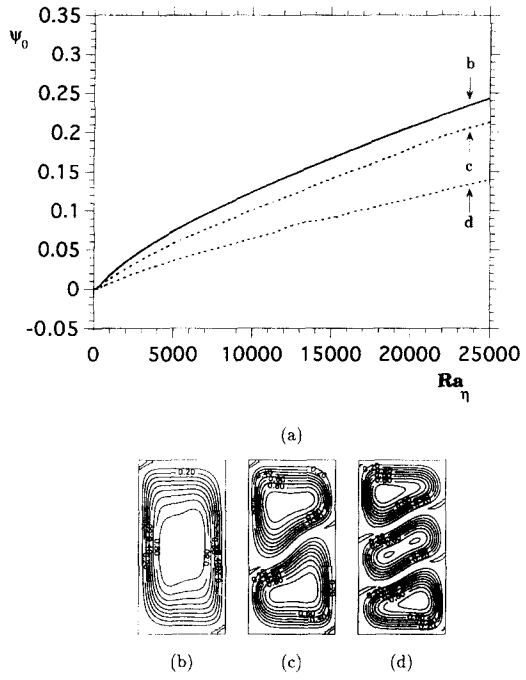

Fig. 3. (a) Bifurcation diagram similar to that in Fig. 1 for $R_\rho = 3$ at large Ra_η. (b–d) Flow patterns at selected points in Fig. 3(a).

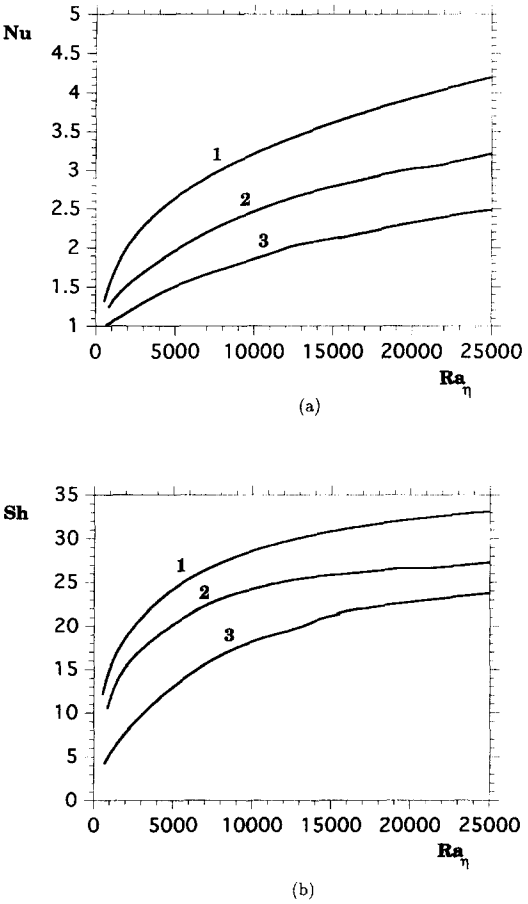

Fig. 4. Plot of the Nusselt number (a) and Sherwood number (b) as a function Ra_η along the branches of Fig. 3(a).

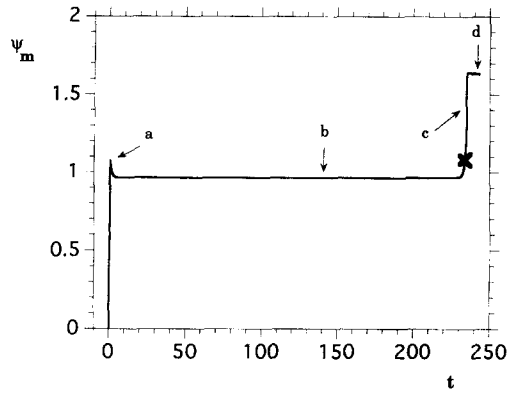

Fig. 5. Maximum of the streamfunction ψ_m as a function of time for $R_\rho = 3$ and $Ra_\eta = 2.37 \times 10^4$.

gration was continued, because no stable two-cell pattern was found in Fig. 3(a). Eventually, the two-cell pattern becomes unstable, weakening the lower cell [Fig. 6(c)] and relatively quickly the one-cell pattern [Fig. 6(d)] is reached which remains steady, consistent with Fig. 3(a).

At $t = 0$, a discontinuity in the temperature distribution at the vertical boundaries occurs. Since Nu is evaluated at the vertical boundaries, it is not defined at $t = 0$. As the four-cell pattern is formed, Nu quickly falls to a value of about 1.9. Subsequent transitions, leading to the two-cell and the final one-cell pattern, cause Nu to increase for the reasons described above. Similarly, the Sherwood number increases with each transition to fewer cells. The final values of Nu and Sh for the two-cell and one-cell solutions agree well with the values that can be obtained from Fig. 4 at $Ra_\eta = 2.37 \times 10^4$. Small differences in the numerical values occur because of the different grid sizes used in the calculations ($25 * 41$ for the calculation of the steady branches and $49 * 81$ for the time dependent results).

The correspondence between the two-cell pattern in Figs. 3(c) and 6(b) is striking. Actually, the time dependent two-cell solution proved to be a very close approximation to the steady-state solution at the two-cell branch in Fig. 3(a). Using the former as a steady-state approximation for the continuation method, a steady-state was reached within three Newton iterations. From Fig. 5 it can be seen that the unstable two-cell solution is physically relevant, because it will be observed for a long time. Since time is scaled with the thermal diffusion time, which is in the order of a day for typical experimental configurations, the two-cell solution may be present for a much longer time-period, i.e. about $100H^2/\kappa_T$ [s]. As the salt diffusion time scale $\tau_S = H^2/\kappa_S$ based on the height of the container has this order of magnitude, the instability of the two-cell steady solution in Fig. 3(c) is likely to be related to intercellular salt diffusion. In Fig. 7 the vertical profile of the salt field ($S(A/2, z)$) at the middle of the container is shown both for the two-cell unstable steady state (drawn line) and at the marked

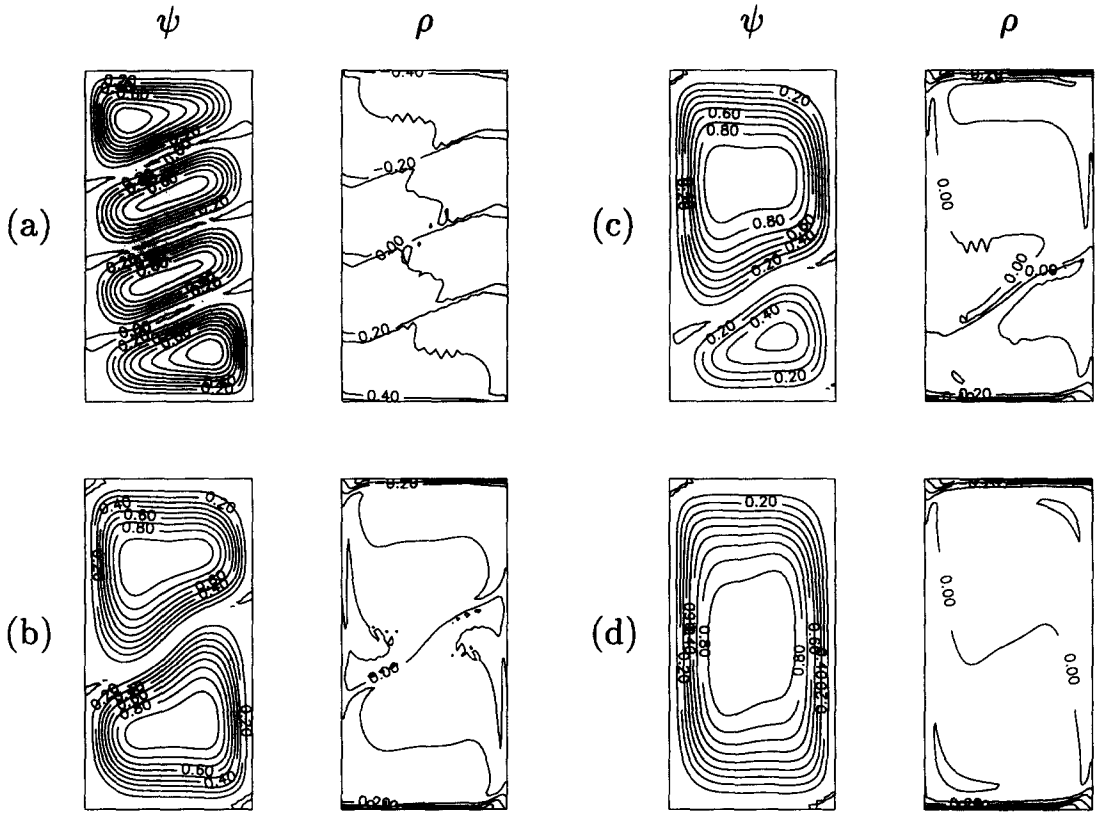

Fig. 6. Plot of the stream function and the density at selected points in Fig. 5.

point in Fig. 5 (dotted line). Indeed, the characteristic length scale over which the salinity difference between both layers exists is of the order H.

However, when the growth factor ($\lambda = 6.78 \times 10^{-2}$) —calculated by solving the linear stability problem of the two-cell steady state—is considered, this value gives a time scale much smaller than τ_S. What actually happens is observed from the flow pattern of the most unstable mode [Fig. 8(a)] and the difference between the time dependent flow and the two-cell steady solution [Fig. 8(b, c)] at different times. At the beginning of the quasi-steady regime, the difference solution

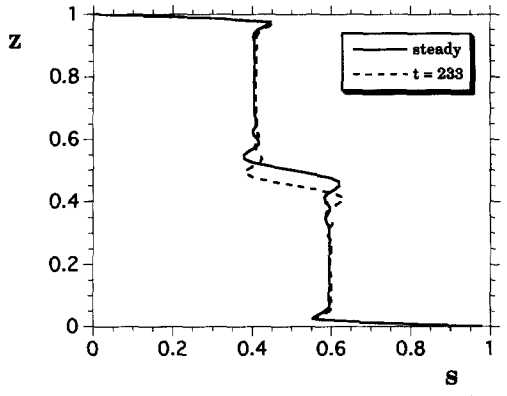

Fig. 7. Vertical profile of the salinity field $S(A/2, z)$ for the two-cell steady-state of Fig. 3(c) and that of the time-dependent state at the marked point in Fig. 5.

[Fig. 8(b)] contains more modes than the most unstable mode, in particular a four-cell pattern. It appears that a long preconditioning phase is necessary to filter out the components of the stable modes. Once these modes have decreased in magnitude [Fig. 8(c)], the instability of the two-cell flow pattern sets in. This instability occurs indeed on a time scale set by λ as was confirmed by perturbing the two-cell steady-state with the unstable mode of a very small positive amplitude and following the evolution by time integration. Exponential growth was observed immediately; the growth factor was computed as 6.95×10^{-2}, very close to the value of λ. If one perturbs the steady-state with the same perturbation pattern, but with a negative amplitude (this is also an eigenvector), the same instability develops and the lower cell is strengthened.

The flow development as described above depends on the value of Ra_η. We performed another transient run, at much smaller $Ra_\eta = 5.0 \times 10^3$. In Fig. 9, a comparison between small and large Rayleigh number initial flow development is shown as a sequence of plots of the streamfunction. At small Ra_η, convection cells form at the lower and upper wall and spread out into the cavity [Fig. 9(a–d)]. Further integration in time shows that a two-cell solution appears which approaches the unstable two-cell steady solution [as in Fig. 3(c)]. At large Ra_η, two cells form in the center and the two cells close to the horizontal walls [Fig 9(e–h)] do not extend downward. The time scale for

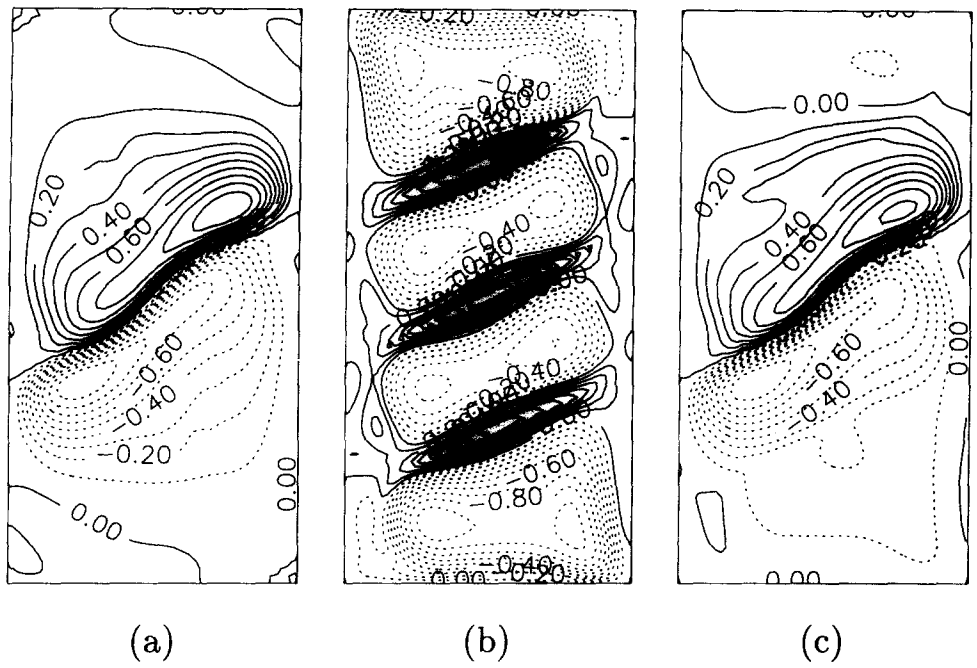

Fig. 8. (a) Plot of the streamfunction of the eigenvector corresponding to the most unstable mode of the two-cell branch ($Ra_\eta = 2.37 \times 10^4$). (b) Difference of the streamfunction of the transient state at $t = 7.92$ and the steady-state. (c) Same as (b), but at $t = 2.29 \times 10^2$.

which the evolution in Fig. 9(a–d) is shown is about a factor 10 slower than that of the development shown in Fig. 9(e–h). Clearly, the main difference between the large and small Rayleigh number transients is the appearance of the four-cell state.

4. BOUNDARIES BETWEEN DIFFERENT FLOW REGIMES

In ref. [11] it is shown that in a container with the same boundary conditions and aspect-ratio as used in our model, different steady-state flow regimes exist, depending on the values of Ra_T and R_ρ. In this section, we try to identify the boundaries between the qualitatively different flow regimes as paths of particular bifurcation points of the underlying dynamical system.

For example, the results in ref. [11] suggest that the unicellular thermally dominated solution no longer exists at larger buoyancy ratio, where cells form simultaneously. A boundary between regimes III (the simultaneously formed layer flow regime) and IV (the unicellular flow regime) apparently exists. We will approach this boundary from the results in Fig. 3(a), where three solution branches were computed up to very large Ra_η. At four fixed values of Ra_T, the flow pattern at the one-cell branch was continued up to larger Ra_S, thereby increasing the buoyancy ratio. For each of these cases, the unicellular flow becomes unstable at a critical value of the buoyancy ratio through a pitchfork bifurcation. The path of this bifurcation in the (Ra_T, Ra_S) plane is plotted in Fig. 10. At larger Ra_T, the value of the buoyancy ratio is of the order 10, which is reasonably in agreement with the experiments in ref. [11]. This value may depend on the Lewis number, actually it is close to the square root of it, but this is not further explored here. The result in Fig. 10 strongly supports that the boundary between region III and IV can be identified as the instability of the unicellular flow.

However, even in the unicellular flow regime, layered flow patterns with a much smaller scale may be observed for a long time. As an example we present (Fig. 11) the transient flow for $R_\rho = 6$ and again $Ra_\eta = 2.37 \times 10^4$. The location of the trajectory in the (Ra_T, Ra_S) plane is also indicated in Fig. 10. A flow pattern with vertical lengthscale η appears after some time, but changes into a four-cell solution. The vertical distribution of fluid properties in the four-cell solution compares qualitatively well with the case of $R_\rho = 3$: convection cells are separated by thin interfaces.

To the left of the drawn curve in Fig. 10, the one-cell solutions no longer exist as stable steady-states. When the points on the curve are continued towards smaller values of Ra_T, while fixing Ra_S, region III is explored. The buoyancy ratio is increased further along this path in parameter space. However, along each computed path, an enormous amount of bifurcation points and limit points appear, similar to that found in the small buoyancy ratio regime at large Ra_S [15–17]. Computationally, it became too expensive to investigate these bifurcation structures in detail. However, the results in ref. [15] suggest that indeed, multicellular flow patterns may exist as steady-states. These states appear due to a combined effect of advection of salt and the appearance of stagnant flow

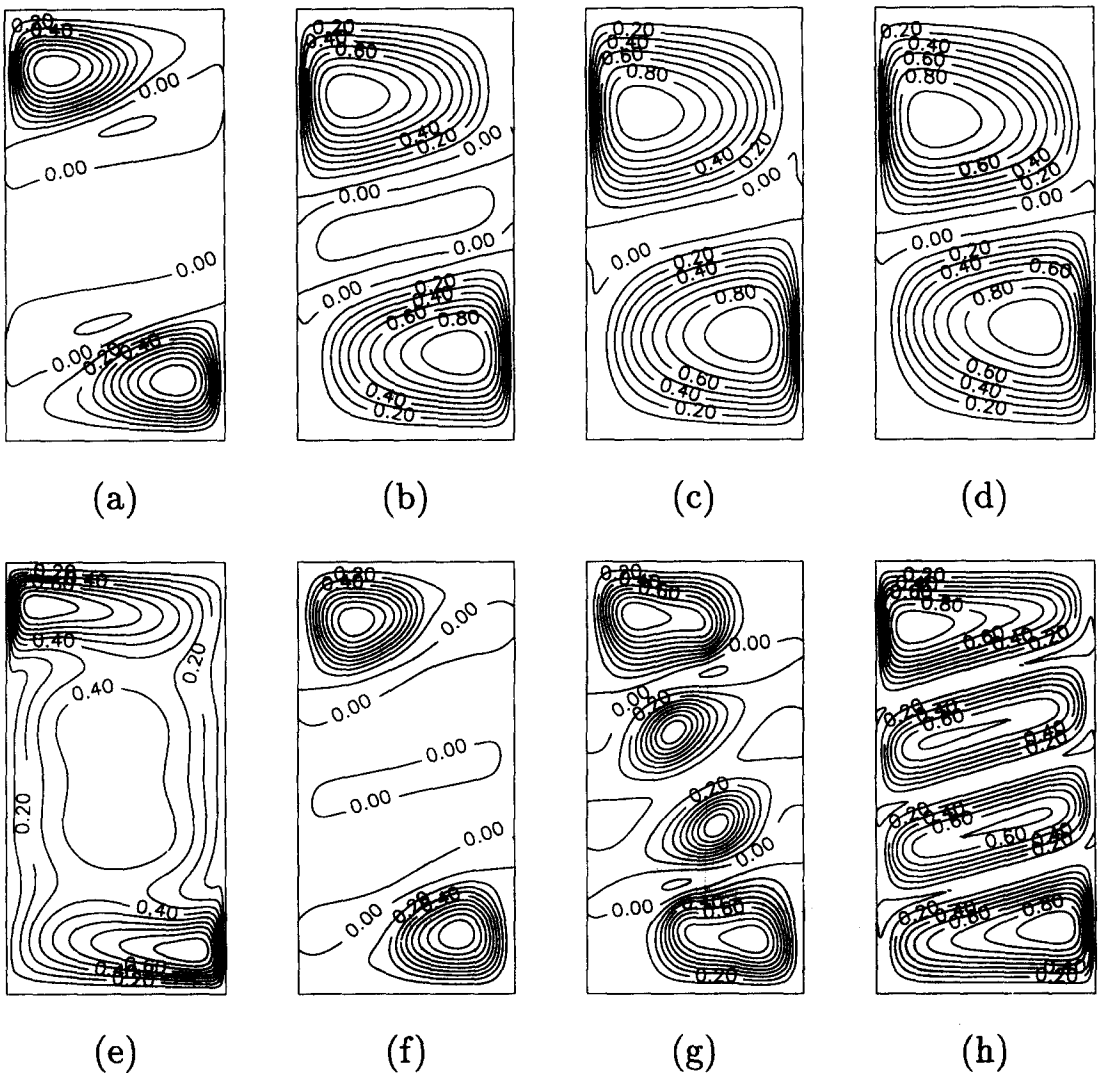

Fig. 9. Comparison of initial flow development for small $Ra_\eta = 5.0 \times 10^3$ (panels a–d) and large $Ra_\eta = 2.37 \times 10^4$ (panels e–h).

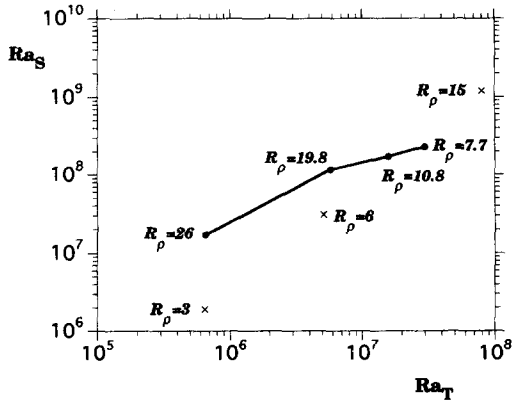

Fig. 10. Path of the bifurcation point corresponding to the instability of the unicellular flow. Also indicated are the locations where trajectories were computed (crosses).

regions when the forcing decreases, which are filled up with cells when the forcing increases. These states may be unstable, as in ref. [15], but they might be physically relevant, because also a preconditioning mechanism may be necessary for the instability to occur. With respect to the steady-state structure, regimes II and III cannot be clearly distinguished, since solution branches corresponding to both regimes likely exist in the same region of parameter space.

Characteristic of the patterns found in regime II is their asymmetry with respect to the center of the cavity [11]. This indicates that these patterns are associated with asymmetric branches, appearing through symmetry breaking bifurcations from the symmetric branch. As an example of such an asymmetric pattern, the evolution of the flow for $R_\rho = 15$ and $Ra_\eta = 2.37 \times 10^4$ is shown in Fig. 12. The location of

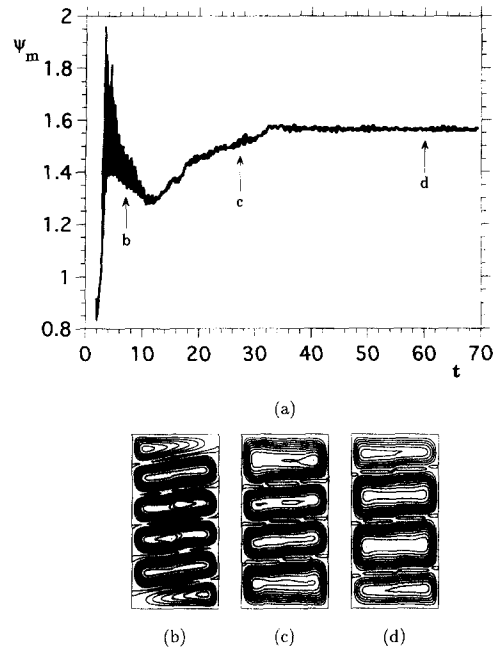

Fig. 11. (a) Plot of the maximum of ψ as a function of time for $R_\rho = 6$ and $Ra_\eta = 2.37 \times 10^4$. (b–d) Flow patterns at selected points in Fig. 11(a).

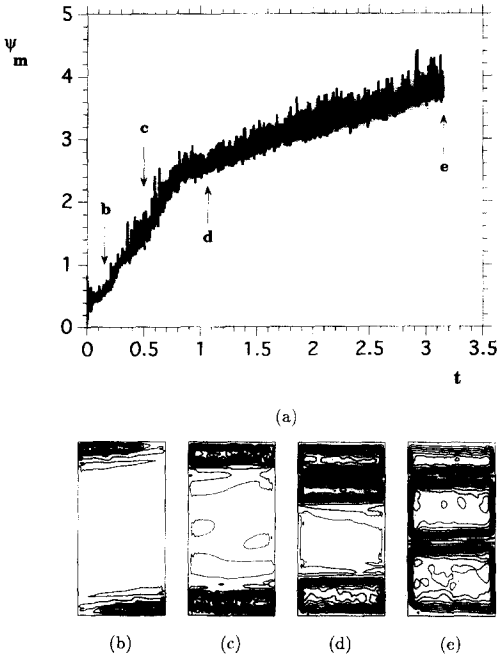

Fig. 12. Same as Fig. 11, but for $R_\rho = 15$.

the trajectory in the (Ra_T, Ra_S) plane (indicated in Fig. 10) is to the left of the curve bounding the unicellular flow regime. The numerical resolution of this particular simulation was increased to a $50 * 100$ grid (and the initial stages were checked with grids up to $150 * 300$), because small scale structures appear during the initial stages of evolution. Even with this high resolution, the flow development is quite irregular [Fig. 12(a)] and certainly no steady-state has been reached at the end of the computation. The evolution of the flow pattern [Fig. 12(b–e)] is similar to the one observed in ref. [11] in the successively formed layer flow regime. Cells appear near the upper and lower boundary, where well mixed layers develop. At first these cells appear symmetrically, but later an asymmetry develops as also seen in experiments. The lower cell remains well as a whole, whereas in the upper area two separate layers develop.

According to the experiments in ref. [11], regime I is characterized by a very weak flow concentrated near the horizontal walls. This weak flow is similar to that on the primary solution branch [Figs. 1 and 2(a)], which is obtained by continuation of the zero flow solution to larger thermal forcing. As regime II is associated with the occurrence of asymmetric solutions, the limit point L_1 in Fig. 1 is a good candidate as a boundary of different qualitative behavior, since below this point only symmetric solutions exist. However, because of the large computational effort we have not followed the path of the limit point in parameter space.

5. DISCUSSION

In this paper, we attempted to identify the different flow regimes as found in the experiments of ref. [11] by the paths of the bifurcation points of the governing system of differential equations. This has been partly successful, since basically only the boundary between region III and IV can be clearly identified and a good guess is obtained for that between region I and II. The boundary between regimes II and III is not that clearly defined because of the abundance of bifurcation points in this area of parameter space. The precise reason for this is unclear, but apparently the symmetric flow is very sensitive to asymmetric perturbations.

However, many interesting results have been obtained during this attempt. Above some critical value of Ra_η, associated with the limit point marking the boundary between regimes I and II, multiple steady-states were found over a large region of parameter space. In regime IV, the low buoyancy ratio regime, the structure of attractors is quite simple since only three branches extend to a very large Ra_η. The evolution of the flow towards the unicellular stable flow was shown to remain for a long time near one of the unstable states before it undergoes an instability. This means that the unstable states are physically relevant, since they may be observed for a very long time. In principle, this instability can be due to the shear in the basic state or it can be buoyancy driven, whereby double diffusion may play a role. To investigate whether shear might be a candidate, the Richardson number defined by

$$Ri = -\frac{\partial \rho}{\partial z} \Big/ \left(\frac{\partial u}{\partial z}\right)^2$$

where u denotes the horizontal component of the velocity was computed. The values of Ri near the interface between the two cells [Fig. 6(b)] are quite large (>1). Hence, it is unlikely that shear will drive the instability. Also the structure of the most unstable mode [Fig. 8(a)] does not suggest a shear driven instability, since smaller perturbation structures would be expected.

It turns out to be difficult to show why the most unstable mode, as in Fig. 8(a), and the corresponding perturbations in the other quantities get amplified through a buoyancy driven mechanism. However, when the flow perturbation [Fig. 8(a)] is superposed on the steady-state flow [Fig. 3(c)], the upper cell gets amplified, and the intensity of the lower cell is diminished. Hence, there will also be asymmetric transport of heat and salt and apparently this leads to amplification of the perturbations. During the transition from the two-cell solution to the final one-cell solution, there is little sign of interface breakdown, at least not in the early stages of the transition. As the interface migrates downwards, both the strength of the salinity gradient and the thickness of the interface remain nearly the same (Fig. 7).

Even when the parameters are chosen in the unicellular flow regime, it should be stressed that for large enough Ra_T, cellular structures with lengthscales much smaller than that of the container size may be observed for a long time. In other words, the signatures of regime III may already be present in the trajectories in regime IV. These patterns likely are related to unstable steady-states just as in the case $R_\rho = 3$. Similarly, at small Ra_T signatures of the successively formed flow regime can be found in the trajectories in regime IV. Hence, these results indicate that it should be difficult to distinguish the different flow regimes experimentally, in particular the boundary between the region II and III. Indeed, [11] and [3] give overlapping intervals for the buoyancy ratio corresponding to the two regimes. The critical value of Ra_η as proposed by ref. [3] cannot be identified here as a path of a particular bifurcation point.

The boundary between regions I and II is likely to be related to the limit point on the asymmetric branches appearing from the first pitchfork bifurcation. One might ask, whether this pitchfork bifurcation is related to the double diffusive instability of a parallel flow in the limit of a vertically unbounded layer [8]. With $A = 1/2$ the steady-state solutions near this pitchfork are not a good approximation to the parallel flow in an infinite vertical slot. We followed the path of the primary bifurcation point (P_1 in Fig. 1) towards smaller A, and although the steady-state flow became more and more parallel, the primary bifurcation was always to an asymmetric state and not to an array of cells. These results clearly show that the primary bifurcation point and the point of instability of the parallel flow in a narrow slot are not related; the upper and lower walls appear to play a dominant role in the instability of the flow.

As a summary, it appears that the underlying dynamical structure of the attractors in this particular case does not help to understand the observed flow patterns as much as one could hope for. Several aspects of the flow in the experiments, other than in ref. [11], are neglected in this study, such as impervious horizontal walls and a time-dependent heating function at the sidewall. The influence of these aspects can only be studied by direct numerical simulation using a high resolution. Although in this case, only steady patterns exist for which the salt is homogeneous, it is expected that the attractors computed with fixed salt field at the top and bottom 'deform' to slow regions in phase space. In this case, the patterns found above (e.g. the unicellular flow), may appear as quasi-steady-states. However, certainly at higher buoyancy forcing, very complicated trajectories can be expected.

Acknowledgements—All computations were performed on the CRAY C98 at the Academic Computing Centre (SARA), Amsterdam, the Netherlands within the project SC212. Use of these computing facilities was sponsored by the Stichting Nationale Supercomputer faciliteiten (National Computing Facilities Foundation, NCF) with financial support from the Nederlandse Organisatie voor Wetenschappelijk Onderzoek (Netherlands Organization for Scientific Research, NWO). The authors thank Jeroen Molemaker for the use of the explicit CFD code and for comments on the results.

REFERENCES

1. R. W. Schmitt, Double diffusion in oceanography, *Ann. Rev. Fluid Mech.* **26,** 255–285 (1994).
2. S. A. Thorpe, P. K. Hutt and R. Soulsby, The effect of horizontal gradients on thermohaline convection, *J. Fluid Mech.* **38,** 375–400 (1969).
3. C. F. Chen, D. G. Briggs and R. W. Wirtz, Stability of thermal convection in a salinity gradient due to lateral heating, *Int. J. Heat Mass Transfer* **14,** 57–65 (1971).
4. J. Tanny and A. B. Tsinober, The dynamics and structure of double-diffusive layers in sidewall-heating experiments, *J. Fluid Mech.* **196,** 135–156 (1988).
5. R. A. Wirtz, D. G. Briggs and C. F. Chen, Physical and numerical experiments on layered convection in a density-stratified fluid, *Geophys. Fluid Dyn.* **3,** 265–288 (1972).
6. H. E. Huppert and J. S. Turner, Ice blocks melting into a salinity gradient, *J. Fluid Mech.* **100,** 367–384 (1980).
7. C. Jeevaraj and J. Imberger, Experimental study of double-diffusive instability in sidewall heating, *J. Fluid Mech.* **222,** 565–586 (1991).
8. S. Thangam, A. Zebib and C. F. Chen, Transition from shear to sideways diffusive instability in a vertical slot, *J. Fluid Mech.* **112,** 151–160 (1981).
9. O. S. Kerr, Heating a salinity gradient from a vertical sidewall; linear theory, *J. Fluid Mech.* **207,** 323–352 (1989).
10. O. S. Kerr, Heating a salinity gradient from a vertical sidewall: nonlinear theory, *J. Fluid Mech.* **217,** 529–546 (1990).
11. J. W. Lee, M. T. Hyun and Y. S. Kang, Confined natural convection due to lateral heating in a stably stratified solution, *Int. J. Heat Mass Transfer* **33,** 869–875 (1990).
12. J. W. Lee and J. M. Hyun, Double diffusive convection in a cavity under a vertical solutal gradient and a horizontal temperature gradient, *Int. J. Heat Mass Transfer* **34,** 2423–2427 (1991).

13. H. A. Dijkstra, On the structure of cellular solutions in Rayleigh–Bérnard–Marangoni flows in small-aspect-ratio containers, *J. Fluid Mech.* **243,** 73–102 (1992).
14. H. A. Dijkstra, M. J. Molemarker, A. Van der Ploeg and E. F. F. Botta, An efficient code to compute non-parallel flows and their linear stability, *Comput. Fluids* **24,** 415–434 (1995).
15. E. J. Kranenborg and H. A. Dijkstra, The structure of (linearly) stable double diffusive flow patterns in a laterally heated stratified liquid, *Phys. Fluids* **7,** 680–682 (1995).
16. N. Tsitverblit and E. Kit, The multiplicity of steady flows in confined double-diffusive convection with lateral heating, *Phys. Fluids A.* **5,** 1062–1064 (1993).
17. N. Tsitverblit, Bifurcation phenomena in confined thermosolutal convection with lateral heating: commencement of the double-diffusive region, *Phys. Fluids A.* **7,** 718–736 (1995).